PUBLICATIONS OF THE ASTRONOMICAL SOCIETY OF THE PACIFIC, **118**: 907–919, 2006 July

Improvements to the Image Processing of *Hubble Space Telescope* NICMOS Observations with Multiple Readouts[1]

V. FADEYEV, G. ALDERING, AND S. PERLMUTTER

Physics Division, Lawrence Berkeley National Laboratory, 1 Cyclotron Road, Berkeley, CA 94720; vafadeyev@lbl.gov, galdering@lbl.gov, saul@lbl.gov

Received 2005 July 3; accepted 2006 May 31; published 2006 June 28

ABSTRACT. We report on improvements made to the standard NICMOS processing pipeline. The calculation of the uncertainties on the signal accumulation rate has been modified to include the statistical correlations between the consecutive readouts. This leads to a ~30% correction in the photometric weight of individual pixels containing faint objects. In order to correct a problem with the existing cosmic-ray rejection algorithm, we have developed and implemented a joint fit procedure, where the accumulating signal is fit as linear functions of time with the same rate both before and after the cosmic-ray (CR) impact. This procedure leads to significantly smaller uncertainty in the count rate for pixels affected by CRs. We also show that regions neighboring CRs found by the standard NICMOS pipeline are systematically brighter. This interpixel correlation substantially increases the footprint of CR impacts and is treated for the first time by our new pipeline. The new processing is most relevant for photometry from deep observations of faint targets, for which accurate, optimal, and unbiased uncertainty estimates are important. We present examples of these improvements for deep NIC2 images of a high-redshift supernova from the Supernova Cosmology Project. The net improvement is a factor of 2 reduction in the number of 3 σ photometric outliers.

1. INTRODUCTION

The Near-Infrared Camera and Multi-Object Spectrometer (NICMOS; Thompson et al. 1998) is one of the most successful instruments of the *Hubble Space Telescope* (*HST*), providing infrared images free of atmospheric influence. The instrument data have contributed to more than 100 publications in the last 5 years.

At the heart of the instrument are three 256 × 256 HgCdTe infrared arrays manufactured by Rockwell Scientific (Hodapp et al. 1992; Skinner et al. 1998). Imaging with these arrays is different from imaging with CCD-based devices in several aspects. The two features that are most relevant to this paper are the existence of an operation mode with multiple nondestructive readouts (MULTIACCUM), and a relatively high readout noise (26 e^- vs. 5 e^- typical for the CCDs; Schultz et al. 2005; Heyer & Biretta 2005).[2] Common to both types of arrays is significant cosmic-ray (CR) pollution caused by operation in space (Calzetti 1997). The MULTIACCUM readout mode allows one to follow the time development of the signal in a given pixel (Schultz et al. 2005). This information can be used to extract the source count rate from the time development of the signal, as is done in the NICMOS data-processing pipeline. The information from multiple readouts effectively reduces the impact of the large readout noise and gives a better count-rate estimate than the simple difference of the final and initial readouts (Garnett & Forrest 1993; Offenberg et al. 2001; Fixsen et al. 2000; Thompson et al. 1998; Sparks 1998). The timing information also allows one to correct for the CR impacts and potential-well saturation on a per pixel basis (Bushouse 1997).

In this paper, we show that the standard NICMOS pipeline correctly determines the count rate, but not the count-rate uncertainties. The pixel-level uncertainties are important for photometry, as they directly propagate to the estimated uncertainty on the derived magnitude. For some scientific applications, such as cosmological studies, a correct evaluation of the uncertainties is of paramount importance. Even though one can obtain an estimate of the average uncertainty from the rms of the sky pixels, in practice correct implementation of such a measurement is complicated by the large spatial variation of the quantum efficiency across the array and corruption and increased uncertainty for pixels with CR hits.

These considerations motivated us to make several improvements to the NICMOS pipeline processing, which are especially important for studies of faint sources. Our first modification to the pipeline results in a better estimate of the pixel-level count-rate uncertainty. We also report on techniques for improved detection and enhanced suppression of CR hits. All improvements described in this paper are in-

[1] Based in part on observations made with the NASA/ESA *Hubble Space Telescope*, obtained at the Space Telescope Science Institute, which is operated by the Association of Universities for Research in Astronomy, Inc., under NASA contract NAS5-26555. These observations are associated with programs GO-8088 and GO-9075.

[2] This number (26 e^-) is typical for a differenced pair of readouts.

corporated into an IRAF/STSDAS[3]-compatible C program, which we call CALNICCR, originally derived from the standard NICMOS pipeline.

The rest of the paper is organized as follows. In § 2 we discuss a deficiency of the existing error determination and present an improved technique. In § 3 we describe several problems with the treatment of CRs in the standard NICMOS pipeline and then describe our improved procedure for handling CR hits. We show a comparison between the default processing and our own in § 4, followed by our conclusions in § 5.

2. LINEAR FIT AND POISSON SIGNAL CORRELATIONS

The targets of most NICMOS observations do not show variability on the timescale of an exposure. Since *HST* guiding is very accurate (Schultz et al. 2005), we can expect the count rate of the source to be constant in each pixel. Typically, the sky background does not vary during an observation, except when there is a scattered Earthlight at the ends of an exposure (Williams et al. 2000). However, the recommended "`biaseq`" procedure (Mobasher & Roye 2004), designed to remove spurious quadrant bias jumps occurring between readouts, linearizes the time development of the average counts in a quadrant. This procedure therefore removes any changes in the sky background, so the incoming photon flux in any pixel is seen to be constant in time after preprocessing. The response of the HgCdTe arrays has been well characterized (Thompson et al. 1995; Skinner et al. 1998), and nonlinearity corrections are applied in a processing step prior to the count-rate determination (Bushouse 1997). Therefore, it is natural to expect that the readout values in a pixel, y_i, are accumulating linearly with time, $y = a + b$ time. One can then extract the count rate in a pixel, b, by performing a linear fit to the readout values[4] (Bushouse 1997).

For the purpose of the following discussion, it is useful to distinguish two components of the signal, y_i, read out from a detector pixel during the ith readout: a Poisson count P_i due to photon sources, and a Gaussian-distributed readout noise r_i, inherent in the detector and its electronics. The Poisson term includes counts from astronomical objects and from background components, such as "amplifier glow," discussed below. The readout noise introduces a jitter on top of the signal, thereby changing the readout y_i from the true Poisson count P_i: $y_i = P_i + r_i$. The exact value of r_i for an individual readout is not known. It is generally assumed that the electronics function in the same way independently for all readouts. In this case the r_i are uncorrelated, and they have constant standard deviation, R, which can be measured separately using, e.g., bias calibration images.

The signal from the photon sources results in correlation between the readouts, since the signal accumulated by the time of one readout affects the statistics of the following readouts. The correlation coefficient between readouts i and $i + k$ is

$$\mathrm{corr}(i, i + k) = \frac{P_i}{\sqrt{P_i + R^2}\sqrt{P_{i+k} + R^2}} \ . \tag{1}$$

The standard least-squares linear fit formulae for the count rate, which assume statistically independent readout values, are shown in Appendix A. They account for a weighting factor, σ_i, associated with readout y_i. For independent data samples the minimum variance estimate for the weight factors is set equal to the readout variance, $\sigma_i^2 = \mathrm{Var}(y_i) = P_i + R^2$. It is this formalism that is implemented in the standard NICMOS pipeline.

However, as is evident from equation (1), the assumption of statistical independence of the readouts is not strictly true, and is violated to a degree dependent on the relative strength of the Poisson photonic noise and the readout noise. In the limit where the photon counts are small compared to the readout noise, the correlation between the readouts vanishes, and the standard formulae shown in equations (A1)–(A4) become a reasonable approximation.

The NICMOS devices are afflicted by amplifier glow, where the amplifiers positioned at the corners of the four quadrants warm up during each readout and become a source of thermal radiation to which the infrared detectors are sensitive (Skinner et al. 1998). This effect results in deposition of a 10–15 e^- signal in the center of the detector per readout (Schultz et al. 2005) and an order-of-magnitude larger signal in the corners. The size of the effect scales linearly with the number of readouts (Hodapp et al. 1992, 1996).

Both a model of the glow, G, and a model of the dark current, D, are subtracted from each readout prior to the count-rate derivation, but the assigned errors (aforementioned weighting factors σ_i) are derived using the original counts. In the rest of the paper, we use the notation y_i' to indicate the background-subtracted readouts, $y_i' = y_i - (GN_{\mathrm{read}} + Dt_i)$. It is the y_i' values that are used in the linear fit to extract a count rate for a pixel.

For long exposures with over 20 MULTIACCUM readouts the amplifier glow is more significant in the center of the detector than other sources of background photons, such as dark current and zodiacal light, and its variance is comparable to that of the readout noise. In this case the correlations between the readouts become appreciable. The correlations are even more important for bright targets, and for objects imaged in

[3] IRAF is distributed by the National Optical Astronomy Observatory, which is operated by the Association of Universities for Research in Astronomy, Inc., under cooperative agreement with the National Science Foundation. The Space Telescope Science Data Analysis System (STSDAS) is distributed by the Space Telescope Science Institute.

[4] NICMOS arrays exhibit a time- and wavelength-dependent nonlinear behavior. It was first observed in Bohlin et al. (2005) and further investigated in Mobasher & Riess (2005), de Jong et al. (2006), and Bohlin et al. (2006). The correction prescribed in de Jong (2006) involves tuning an image after the pipeline is run, and pixel-level count rates are determined to a first approximation.

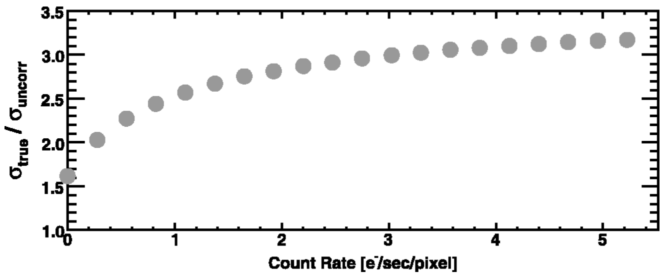

FIG. 1.—Ratio of the true standard deviation of the count rate and that derived according to the uncorrelated linear fit formulae (A2)–(A4) as a function of the count rate. Ignoring the correlated uncertainties leads to significant error on the quoted uncertainties, by a factor ranging from 1.26 for faint objects to about 3.5 for the brightest objects. Using the proper noise value of 19 e^- in the fit would bring the error factor to 1.62 for faint objects.

the corners of the detector, which are more severely affected by the amplifier glow.

Note that NICMOS Instrument Handbook (Schultz et al. 2005) quotes the noise value for a pair of differenced readouts, and it is this value that the standard NICMOS pipeline uses as a noise estimate (value of R in the formulae above). It makes more sense to use the noise per single readout, which is smaller by a square root of 2, in the count-rate derivation for a given pixel. We used a single readout noise value in CALNICCR, and also in the standard pipeline when a comparison of different ways of processing is made.

Given the presence of correlations, one can ask (1) whether the implemented formulae are optimal (giving the smallest uncertainty), (2) whether they are biased, and (3) whether the count-rate uncertainty derived from the fit is correct. To answer the first two questions, we performed Monte Carlo simulations using nominal input parameters: a gain of 5.4 e^- ADU^{-1}, amplifier glow of 15 e^- per readout, readout noise of 19 e^-, dark current of 0.050 e^- s^{-1}, and a MIF1024 (Schultz et al. 2005) readout sequence with 26 readouts.[5]

These simulations indicate that including the correlations in the fit improves the scatter of the count-rate estimate by at most 15% for a background-limited object located in a corner of the array. The improvement is only 3% for a background-limited object at the center of the array. Since our targets are generally near the center of the array, we did not modify the formalism of the count-rate derivation in the NICMOS pipeline. These simulations also indicate that the uncorrelated linear fit does not introduce a bias in the count-rate estimate.

However, the accuracy of the uncertainty assigned to the count rate using the standard method is not sufficiently accurate. The count-rate uncertainty derived according to equations (A2)–(A4), $\sigma_{\mathrm{uncorr}}(b)$, underestimates the true standard deviation, $\sigma_T(b)$. Figure 1 shows the ratio $\sigma_T(b)/\sigma_{\mathrm{uncorr}}(b)$ as a function of the source rate. One can see that the uncertainty derived according to equations (A2)–(A4) underestimates the true standard deviation by a factor of 1.6 for the sky pixels. For pixels with a source rate of 5 e^- s^{-1}, the standard uncertainty estimate is off by a factor of 2.9. The ratio has an asymptotic value of 3.5 for very high count rates.

We note that the large readout noise value used in the standard pipeline can serve as a "fudge factor" alleviating the deficiency of the uncertainty estimates. For instance, if we use 19 e^- as the readout noise value for Monte Carlo data generation and use 26 e^- as the noise value in count-rate reconstruction from the same data, then the aforementioned factor of 1.6 for sky pixels is reduced to 1.3.

In the absence of readout noise, the independent variables are the accumulated differences between the subsequent readouts. After rewriting the formulae via the differences $\delta y_i = P_i - P_{i-1} + r_i - r_{i-1} \simeq P_i - P_{i-1}$, one can estimate the part of the b variance that is due to the correlations. The part of the b variance due to the readout noise can be estimated separately, as an additional independent component. The formalism is shown in Appendix B, formulae (B1)–(B5). We note that this concept has been fully described by Sparks (1998), who derived formulae for the case of unweighted data. The formulae were rederived in Gordon et al. (2005) for *Spitzer* data analysis. They are shown here for completeness, and as a precursor to the more sophisticated case that we address in § 3. We verified the correctness of the formulae (B1)–(B5) with Monte Carlo simulations.

To check the performance of the uncertainty estimates on real data, we constructed a histogram of the values of $b/\sigma(b)$ for images with flat sky background and a small number of astronomical sources. The histogram for such images should be close to a Gaussian with unit standard deviation if the derived uncertainties reflect the true scatter of the sky fluctuations. For data taken with MIF1024 and SPARS64 readout sequences, we see that the distribution of pixel values is close to Gaussian,[6] with a width too narrow by a factor of 1.38 (Fig. 2). We consider this to be a major improvement compared to the factor of 1.61 obtained with the same data using the old formulae (eqs. [A2]–[A4]), resulting in a ∼30% adjustment to the photometric weights for pixels containing faint sources. The histograms for both cases are shown in Figure 2. The remaining 30% deviation from unity could be due to a number of causes, including the accuracy of calibration (flat-fielding, response linearity, readout noise and gain characterization, and systematic bias offsets), or possibly the count-rate ramp-up effect discussed in Bohlin

[5] The number of trials for this and other Monte Carlo simulations reported in this paper are at least comparable to the number of pixels in the NICMOS detectors.

[6] The histograms show some obvious departures from an ideal Gaussian distribution. Real astronomical objects in the images contribute to the high end of the distribution. "Hot" and "cold" pixels, unaccounted for in the bad pixel mask, add to both high and low tails. For these reasons, we fit the Gaussian function to the central region within $\pm 2\ \sigma$ to derive the width. The reduced χ^2 varies between 0.9 and 1.3 in such fits.

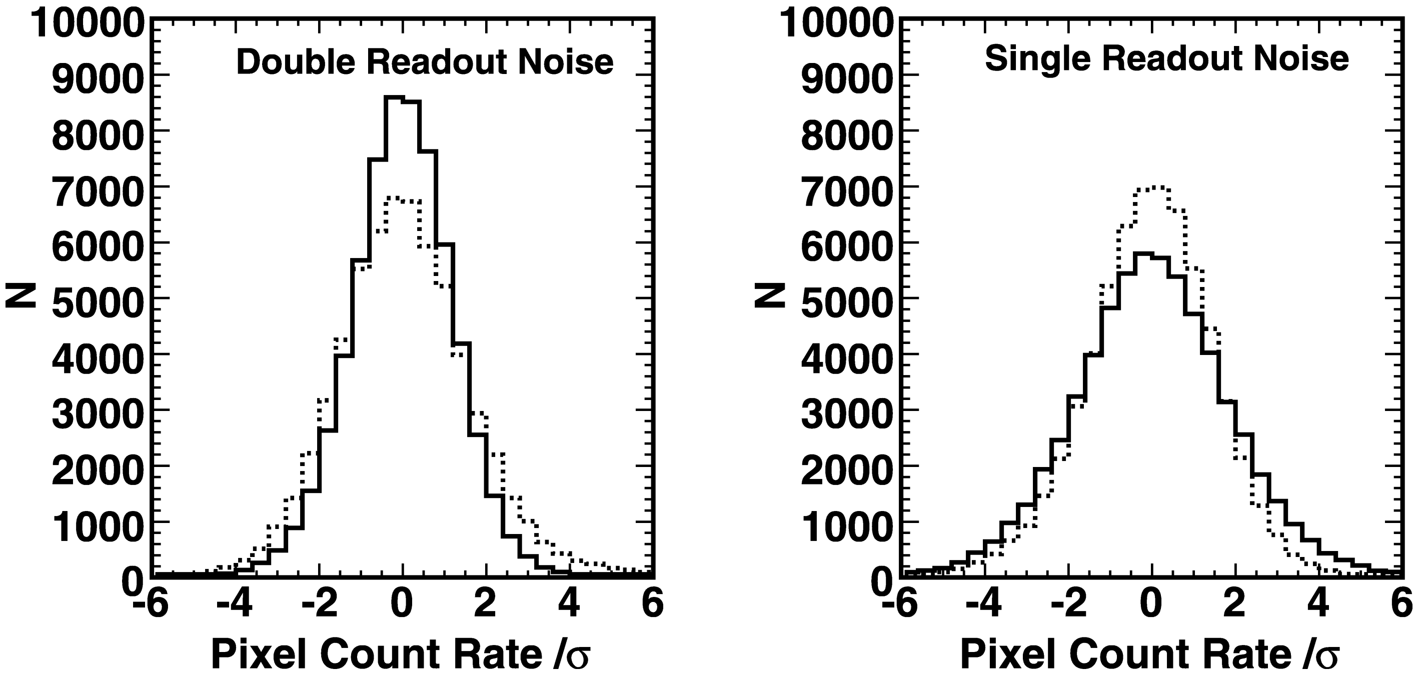

FIG. 2.—Distribution of the pixel count rate divided by its estimated uncertainty in a background-dominated image after sky subtraction. The solid line corresponds to new uncertainty estimates from CALNICCR, accounting for the correlations between different readouts. The dotted line corresponds to the default uncertainty estimates in the NICMOS pipeline. The histogram on the left is made assuming the default readout noise value in the pipeline processing. The histogram on the right is made assuming the proper noise value, which is smaller by $\sqrt{2}$. See text for discussion.

et al. (2005), Mobasher & Riess (2005), de Jong et al. (2006), and Bohlin et al. (2006). Whatever the causes, they also contribute to the factor of 1.61 for the standard pipeline.

3. PIXELS AFFECTED BY COSMIC RAYS

As discussed in § 1, the existence of multiple nondestructive readouts allows one to better account for cosmic rays. In the case of a cosmic-ray hit in a pixel, there is a jump in the signal accumulation with time. It can be identified as an outlier in the consecutive readout differences normalized to the time between the readouts. In the standard NICMOS pipeline, the sequential, uncertainty-normalized differences between the deviation of the readout values from the linear fit are used to find CR candidates:

$$\mathrm{jump}_{i+1} = [y'_{i+1} - (a + bt_{i+1})]/\sigma_{i+1} - [y'_i - (a + bt_i)]/\sigma_i. \tag{2}$$

In the case of a real CR, the deviation is likely to be positive after the jump and negative before the jump. In the standard pipeline, the default threshold for identifying CRs is set to 4 σ (i.e., $\mathrm{jump}_{i+1} > 4$). In principle, the one-sided detection of the jump leads to a bias in an average count rate. However, for reasonable detection parameters, the size of the bias is small, on the scale of a typical count-rate uncertainty in a pixel (see Fig. 5).

3.1. CR Detection Sensitivity

False-positive CR detections will occur, with a likelihood depending on the detection threshold. The jump quantity involves a subtraction of two correlated deviations, each of which is Gaussian-distributed around zero, with the width narrower than unity due to the exaggerated noise value. Without the correlation, the threshold of 4 σ would be similar to a 2.83 σ threshold for a single Gaussian. Using this, one might try to calculate a rough estimate of the fraction of false-positive detections in an exposure by multiplying the number of jump estimates with the single-sided Gaussian tail probability. This naive estimate gives a false CR detection rate of 5.6%, which is significantly different from the 0.015% we obtain with a full Monte Carlo simulation. There are two reasons for this discrepancy—the presence of correlation between the readouts and a wrong noise value—which affects the definition of σ.

There is another way to look at the jump identification in equation (2). We note that in the case of sky pixels the uncertainties for consecutive readouts have similar values, $\sigma_{i+1} \approx \sigma_i$. Therefore, the jump value can be approximated as $[(y_{i+1} - y_i) - b(t_{i+1} - t_i)]/\sigma_{i+1}$. The value in the denominator increases with time, whereas the difference in the numerator

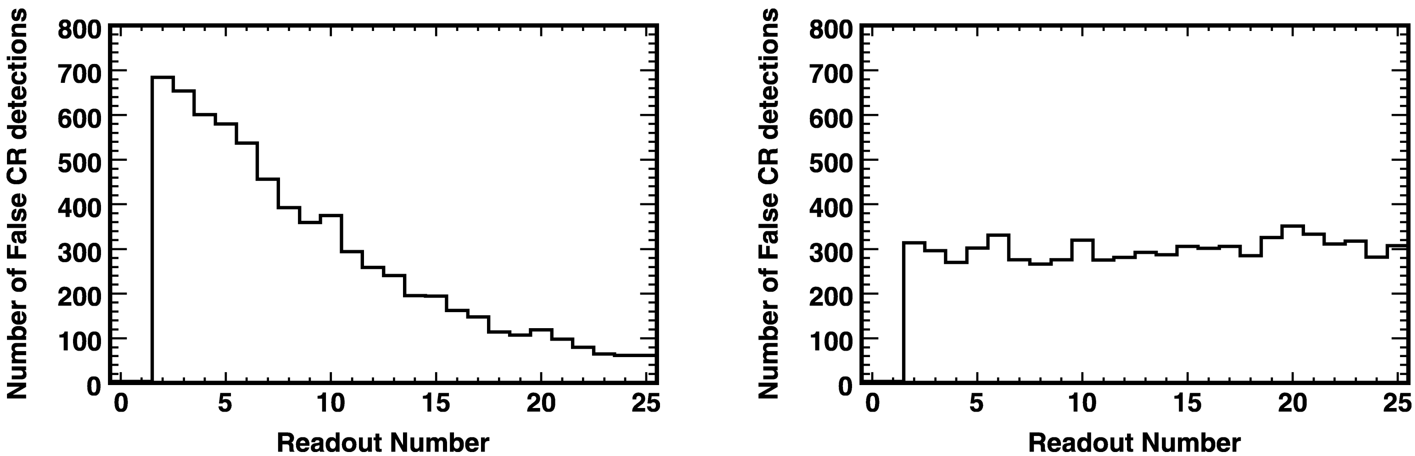

FIG. 3.—Monte Carlo simulation results giving the false-positive CR detection as a function of readout number. The left panel is for the default NICMOS pipeline, and the right panel uses our modified jump definition, as described in eq. (3).

is nearly constant. This leads to a decrease in CR identification efficiency with the number of readouts, as shown in Figure 3 (also see Fig. 4 for the relation between CR detection sensitivity

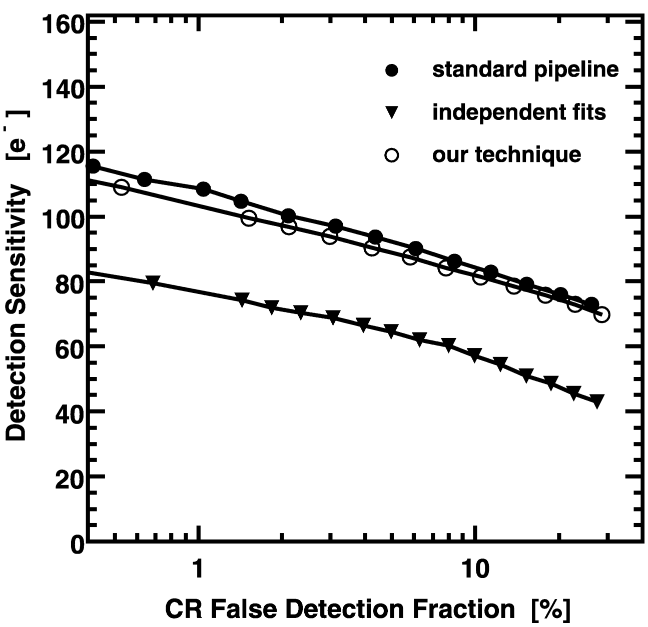

FIG. 4.—CR detection sensitivity as a function of the false-positive CR identification fraction. In this example, the sensitivity is defined as the amount of CR deposition that has a 50% probability of being detected. We show Monte Carlo simulation results for three CR identification and processing methods: (1) the standard NICMOS pipeline, (2) a technique of CR identification and correction by fitting the readout segments before and after a putative CR jump as independent linear functions (Hesselroth et al. 2000; Gordon et al. 2005), and (3) CALNICCR. A lower CR detection sensitivity at the same false-positive rate corresponds to an improved ability to identify weaker CRs. The actual *number* of CRs detected also depends on the distribution function of the charge deposition per pixel per CR.

and a false detection rate of Fig. 3). To remove this undesirable effect, we changed the jump definition for CALNICCR to be

$$\mathrm{jump}_{i+1} = [(y'_{i+1} - y'_i) - b(t_{i+1} - t_i)]/\sigma^*_{i+1},$$
$$\sigma^*_{i+1} = \sqrt{b(t_{i+1} - t_i) + G + D(t_{i+1} - t_i) + 2R^2}. \quad (3)$$

The main difference compared to the previous definition is in the expression for σ^*_{i+1}, which is defined here to reflect the variance in $\delta y' = y'_{i+1} - y'_i$. The change in definition causes the CR detection rate to be time independent in our method (Fig. 3), while maintaining the simplicity of the criterion. Monte Carlo simulations also indicate that this modified CR detection threshold leads to a modest improvement in CR detection sensitivity over the standard pipeline (see Fig. 4).

We note that there is also an alternative method of CR identification used in Hesselroth et al. (2000) and Gordon et al. (2005), in which the jump measurement precision is improved using the values of linear fits to the readouts before and after the jump:

$$\mathrm{jump}_{i+1} = [a_2 + b_2 t_{i+1} - (a_1 + b_1 t_i)]/\sigma^{**}, \quad \sigma^{**} = \sqrt{\delta P_i + R^2}. \quad (4)$$

The quantity δP_i is estimated from the linear fit to readouts prior to the jump candidate. The origin of the expression for the error on the jump estimate, σ^{**}, is not clear; it is similar to our expression for σ^* except for the prefactor for the readout noise variance. Moreover, our equation (3) was derived to be used with the readout values themselves, not the fit functions estimates, where a more complicated error analysis might be necessary. In practice, using equation (4) for selecting a best jump candidate can lead to a modulation of CR detection sensitivity with a readout number.

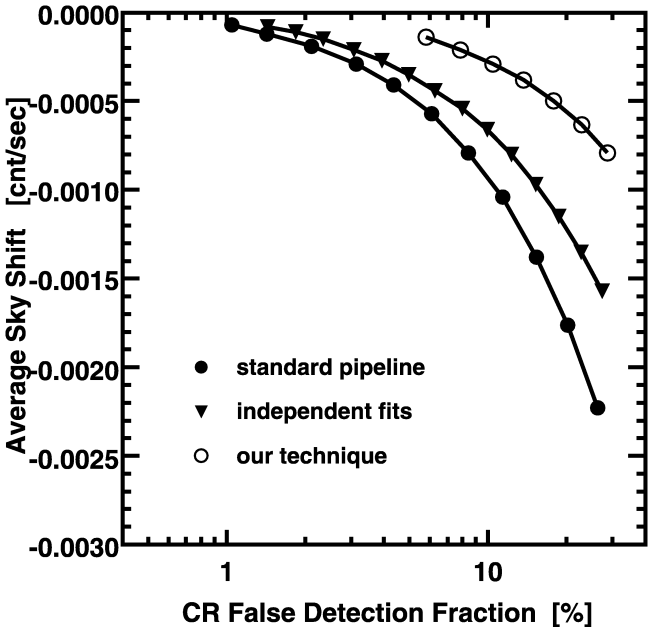

FIG. 5.—Average sky level shift for pixels unaffected by CRs as a function of false-positive CR identification fraction. The shift is due to a bias caused by one-sided jump identification (eqs. [2] and [3]). We show Monte Carlo simulation results for the same three CR identification and processing methods as in Fig. 4: (1) the standard NICMOS pipeline, (2) the technique of Hesselroth et al. (2000) and Gordon et al. (2005), and (3) CALNICCR. A larger shift corresponds to a larger bias. A typical count-rate uncertainty for long exposures is about 0.005 counts s^{-1}.

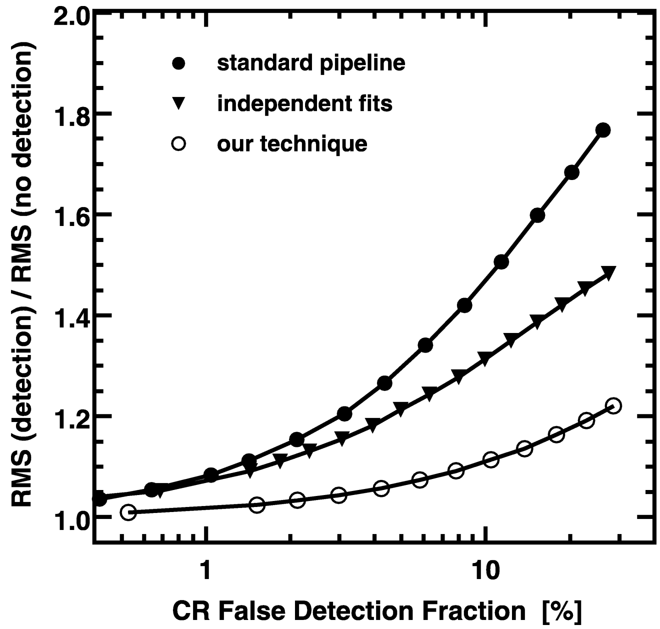

FIG. 6.—Ratio of sky rms with and without CR identification triggered for pixels unaffected by CRs as a function of false-positive trigger rate. We show Monte Carlo simulation results for the same three CR identification and processing methods as in Fig. 4: (1) the standard NICMOS pipeline, (2) the technique of Hesselroth et al. (2000) and Gordon et al. (2005), and (3) CALNICCR. A lower rms ratio at the same false-positive rate corresponds to a better CR correction technique.

Additional techniques can be used to tune the initial selection of CR candidates (as opposed to evaluate their significance). For instance, Hesselroth et al. (2000) used a computationally intensive global likelihood fit to all possible jump scenarios to find the readout containing the most likely CR prior to using the jump-based selection. In Gordon et al. (2005), two-point differences are considered prior to the more careful jump evaluation. We have not included these aspects of Hesselroth et al. (2000) and Gordon et al. (2005) in our Monte Carlo simulations. The uncertainty definition and potential readout number modulation notwithstanding, the idea of using the fit function values to obtain a more precise jump evaluation does lead to an increase in CR detection sensitivity (see Fig. 4).

3.2. Correction for Detected CRs

One needs to account for an identified CR in the pipeline processing of data from a pixel when deriving the count rate and its uncertainty. The standard NICMOS pipeline procedure is to shift the data following the jump on the basis of the two readout values straddling the CR hit, $\delta(y_{i+1}) = y_{i+1} - y_i$, and then refit the new sequence of data to the linear function using formulae (A1)–(A4).

Some of the pixels affected by cosmic rays and processed according to that standard procedure can still be visually identified in images as outliers. We attribute this to the finite precision of the jump measurement. The readout noise contribution can make $\delta(y_{i+1})$ differ from the "true" value of the CR deposition by an amount comparable to the standard deviation of the readout noise. For a given pixel, the difference systematically shifts the values of all post-CR readouts from what would have been an unbiased estimate in the absence of the CR. (The direction of the shift is random.) This affects both the count-rate determination and its assigned uncertainty.

To avoid the CR processing effect described above, we developed a joint fit procedure whereby both the readouts before and after the CR jump are fit to linear functions with the same slope: $y_1 = a_1 + b \times \text{time}$; $y_2 = a_2 + b \times \text{time}$. In this way the fit naturally accounts for the jump $\delta(y) = a_2 - a_1$ on the basis of all available readouts, and there are no artificial shifts in the data. Since we employ a different definition of the jump quantity, a comparison of the performance of the two methods for the same jump threshold is inappropriate. Rather, comparison should be made for thresholds that yield the same rate of false-positive CRs for both methods. For example, we find the same rate of false positives for a threshold of 4.0 in the standard pipeline as for a threshold of 4.37 in CALNICCR. In such a comparison, the effects of false-positive identification—the size

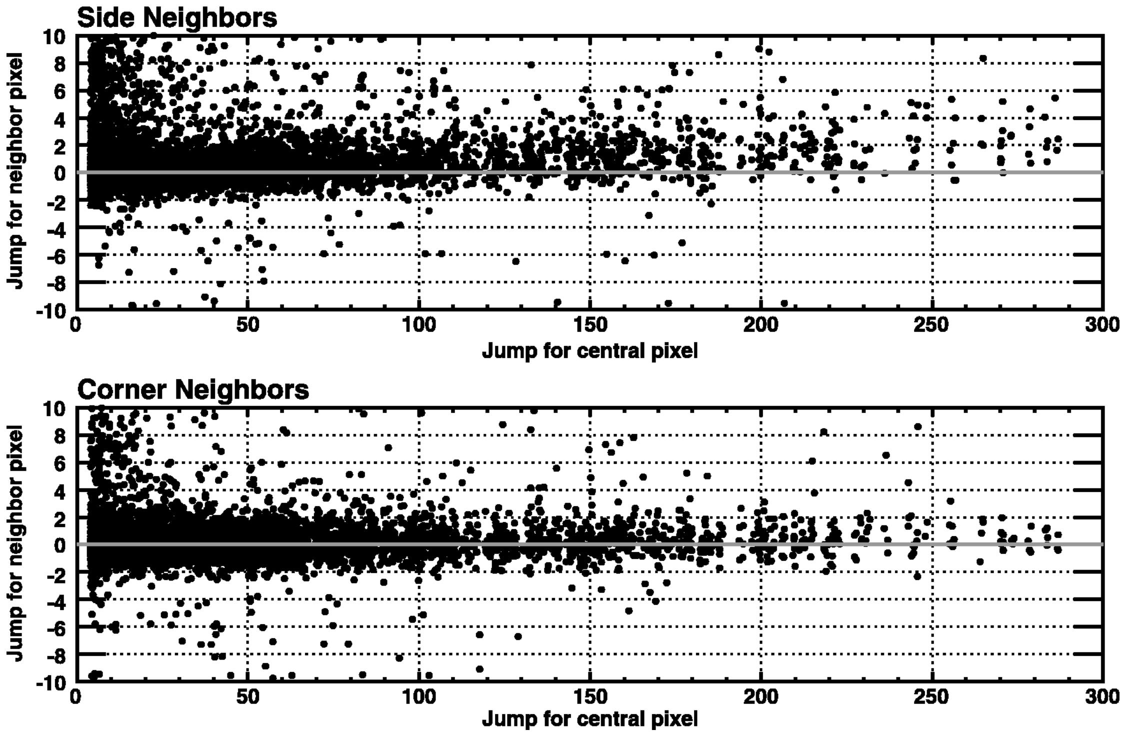

FIG. 7.—Jump value (in units of the standard deviation; see eq. [2]) in the neighboring pixel vs. the primary pixel for an exposure prior to any pipeline correction. *Top*: Side neighbors. *Bottom*: Corner neighbors. All the pixels with an identified CR jump in the primary pixel are plotted if the neighboring jump falls in the selected ordinate range. The range was chosen to focus on the near-threshold behavior of the neighboring pixels, which do feature large jumps in cases when a CR directly interacts with more than one pixel. The statistical information for the plotted data is given in Table 1. To enhance its visibility, the zero-deviation line ($Y = 0$) is shown in gray in these plots.

of the average rate shift and rms spread (Calzetti 1997)—are greatly reduced for our method (see Figs. 5 and 6). The exact formulae for this procedure are presented in Appendix C.

For comparison, the CR correction algorithm included in the *Spitzer* instruments pipeline (Hesselroth et al. 2000; Gordon et al. 2005) evaluates the count rate separately from each of the segments of the readout sequence (partitioned by the CRs), and then the measurements are combined. Our method gives a similar estimate of the count rate, but it is more precise, due to the use of a uniform count-rate estimator (b) for all segments. Indeed, as shown in Figures 5 and 6, our method does achieve a more accurate count-rate estimate, producing a smaller rms and suffering less bias.

We note that in the case of a CR detection the increase in the count-rate uncertainty depends on the time of the impact. The worst-case scenario of a CR occurring in the middle of the exposure increases the uncertainty by about a factor of 2, due to the decreased time axis range of the fit (two halves

TABLE 1
CORRELATION BETWEEN PIXEL JUMP VALUE AND AVERAGE JUMP OF ITS NEIGHBORS

	Side Neighbors			Corner Neighbors		
Primary Pixel Jump ($N\ \sigma$)	Average Neighbor Jump ($N\ \sigma$)	rms (σ)	N Pixels	Average Neighbor Jump ($N\ \sigma$)	rms (σ)	N Pixels
$4 < y < 50$	0.62 ± 0.03	1.87	5155	0.28 ± 0.02	1.44	5682
$50 < y < 100$	0.78 ± 0.05	1.73	1181	0.20 ± 0.04	1.47	1340
$100 < y < 150$	1.13 ± 0.08	1.70	406	0.29 ± 0.08	1.65	486
$150 < y < 200$	1.42 ± 0.14	2.18	251	0.46 ± 0.09	1.48	290
$200 < y < 250$	1.83 ± 0.21	2.07	96	0.70 ± 0.15	1.67	118
$250 < y < 300$	2.42 ± 0.34	1.91	32	0.52 ± 0.15	0.86	34

NOTES.—Statistical information on a correlation between a pixel jump value and an average jump of its neighbors at the same readout. The same data are plotted in Fig. 7.

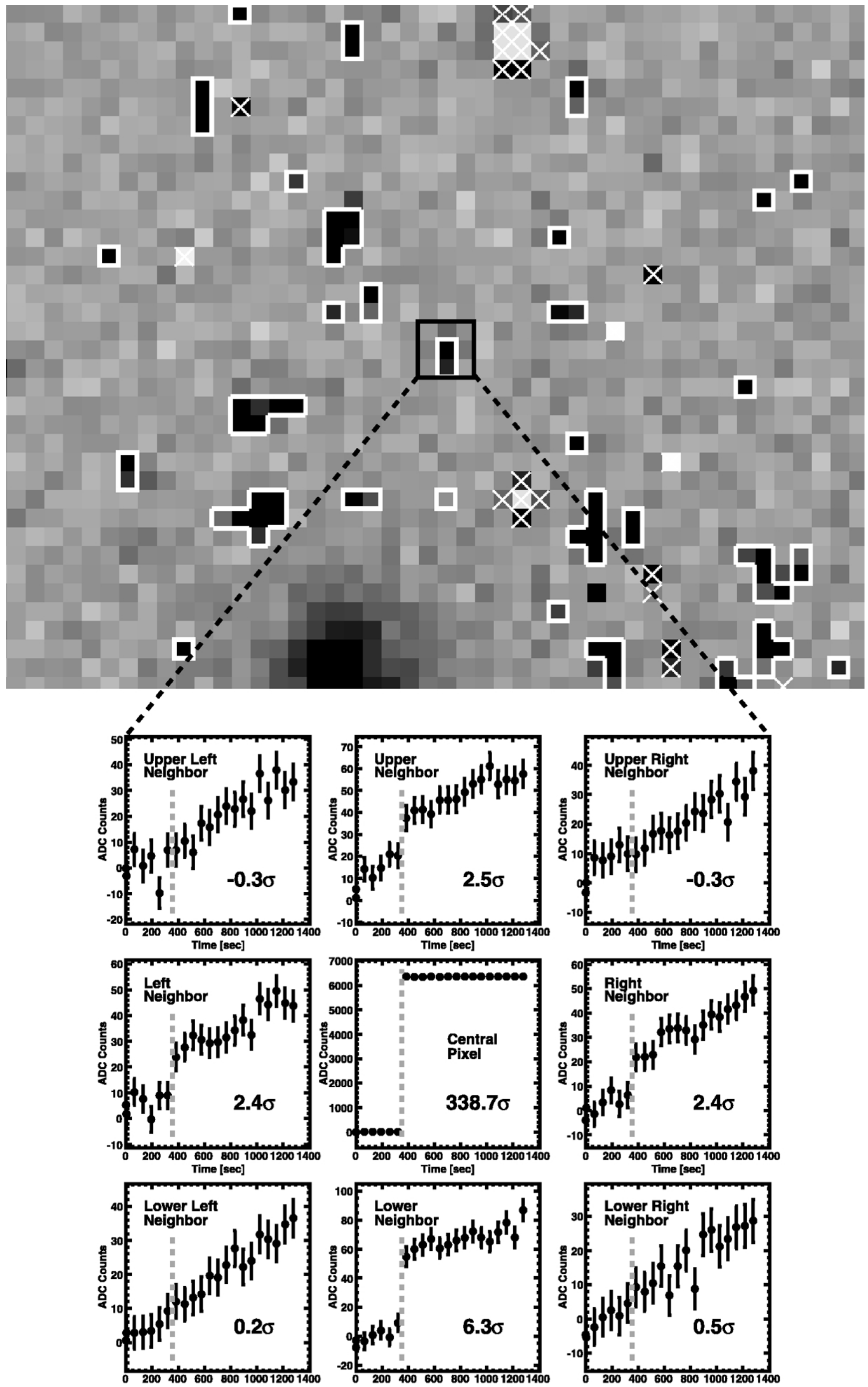

FIG. 8.—Subarray of the reprocessed last readout frame from a NICMOS NIC2 exposure, shown in the top panel of the figure. The darker pixels indicate larger counts, which could be due to cosmic rays. The dark region at the bottom is a field galaxy. The pixels with a CR detection are indicated by white contours. Known bad pixels are crossed. The selected 3 × 3 pixel black box is used as an example in Fig. 9. The box was selected to contain a concentrated CR to illustrate the effect of the primary CR on the neighboring pixels. The time development of the counts in the 3 × 3 box is shown in the bottom panel of the figure. The numbers in the plots show the calculated significance of the jump, occurring at ∼350 s. The jump location is indicated with a gray dashed line for each pixel. The default threshold is 4 σ. Note that only one of the side neighbors of the central pixel is above this threshold (labeled "Lower Neighbor" on the plot subpanel), but several other side pixels are also significantly affected.

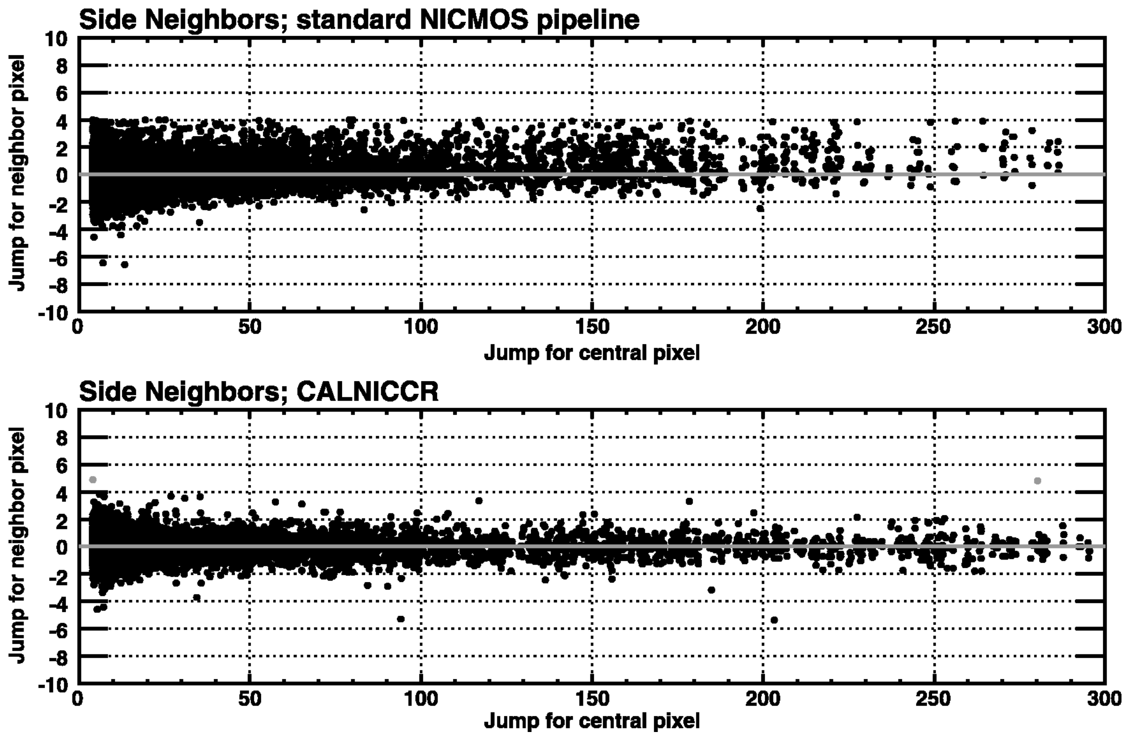

FIG. 9.—Jump value after a pipeline correction vs. the original one for side neighboring pixels. *Top*: Standard NICMOS pipeline, run with jump threshold of 4.00 (see eq. [2]). *Bottom*: CALNICCR, run with jump threshold of 4.37 (see eq. [3]). The thresholds are chosen to have a similar CR rejection performance for the two pipelines. This figure is similar to the top plot in Fig. 7, and it shows the data from the same exposure. The emphasis here is made on the data features after a pipeline correction is applied. The gray points on the bottom plot are due to a single special pixel with extremely peculiar signal time development.

combined are worse than one whole). The "shifting" procedure in the standard NICMOS pipeline does not account for this effect, when calculating the uncertainty.

3.3. CR Correction of Neighboring Pixels

On examination of the processed images, we noted one additional artifact: a number of "sky" pixels adjacent to CR-affected regions visually appeared to be positive outliers. The readout sequences of the neighboring pixels show moderately significant jumps at the same time as the nearby CR-affected pixels. However, as these correlated jumps are below the CR detection threshold, a substantial number of CR-affected pixels are not treated in the standard NICMOS pipeline. The effect is illustrated in Figure 7 and quantified in detail in Table 1, which demonstrate the correlation between the temporally coincident jumps for the neighboring pixels. We note that the correlation is obvious for the side neighbors, but not for the corner neighbors. This pattern is consistent with laboratory studies of HgCdTe array responses to CRs (Offenberg et al. 2001; Figer et al. 2004; Garnett et al. 2004). We show an example of this effect on a real exposure in the Figure 8. This phenomenon may be attributable to CR particles interacting with the array material, possibly spawning secondary particles such as delta electrons and bremsstrahlung radiation.

To remove this bias, we process the images in two passes. The CR identification algorithm is run during the first pass. The time locations of the CR jumps are flagged for each pixel in the array. Then the flags are propagated to the same time locations for the side neighbors. Finally, the second pass of the algorithm is run to refit the data while taking into account the previously identified jumps, and the count rates are extracted for all pixels. This procedure drastically reduces the number of outliers remaining in the images and removes the correlation for side neighboring pixels (Fig. 9).

4. PROCESSING COMPARISON

In this section, we demonstrate the difference between the CALNICCR processing and the standard NICMOS pipeline using real data. First, a visual example is shown, then results from a more quantitative photometric study are given. The data used to illustrate these improvements consist of NICMOS camera 2 (NIC2) images of a high-redshift Type Ia supernova discovered by the Supernova Cosmology Project, obtained with either the MIF1024 or the SPARS64 readout configuration, and having durations ranging from 1026 s (for MIF1024) to 1280 s (for SPARS64). A typical supernova light-curve measurement consists of two to eight such exposures at each epoch. In our typical analysis, the supernova is fit with a model point-spread function

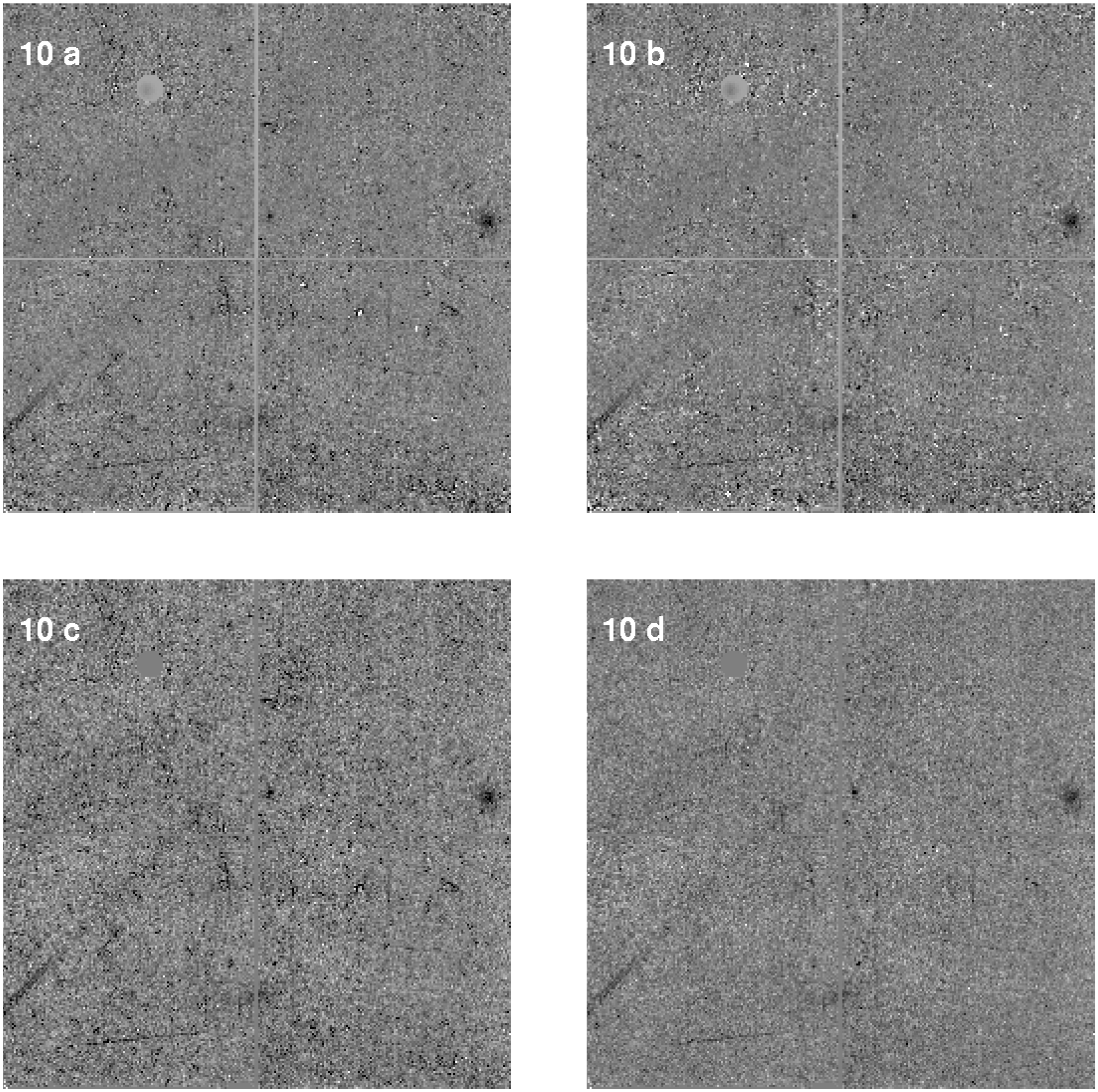

FIG. 10.—NICMOS NIC2 count-rate image of a high-redshift supernova target. The darker pixels correspond to higher count rates. Image (*a*) is obtained with the standard NICMOS pipeline processing, while image (*b*) is obtained with CALNICCR. Images (*c*) and (*d*) correspond to (*a*) and (*b*), except that the sky-subtracted count rates were divided by their estimated uncertainties. The supernova is near the center of the field. There are two faint field galaxies: one on the right-hand side of the picture, and another at about the same distance directly below the supernova. We vetoed pixels along 128th row, 128th and 129th columns, and at the coronagraphic hole location from processing. This created visual peculiarities in the images: middle horizontal and vertical lines and a circle in the upper left quadrant. The 45° streak in the lower left quadrant is a diffraction spike from a star outside the field.

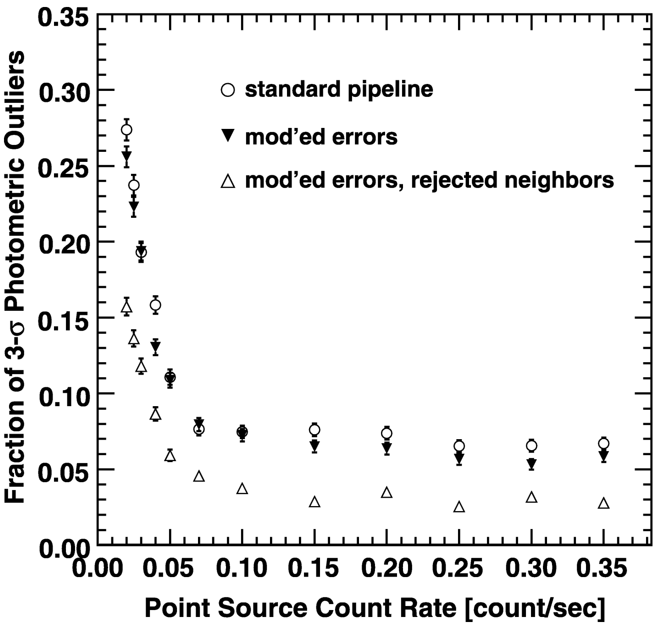

FIG. 11.—Fraction of photometric 3 σ outliers as a function of the input flux for the standard pipeline (*open circles*) and CALNICCR (*filled circles*). Also shown is the intermediate case, in which only the uncertainty estimate is modified (*filled triangles*).

(PSF), and the underlying galaxy is removed using a combination of modeling and reference images. The modeling region can easily extend over an 11 × 11 block of pixels; 10%–50% of these pixels are likely to have suffered a CR hit during one of its exposures at a given epoch. Thus, accurate uncertainties and proper treatment of CRs is critical for obtaining a robust supernova light-curve measurement suitable for measuring the accelerating expansion of the universe.

We show an example of the effect of our processing in Figures 10*a* and 10*b*. By visual examination of the same exposure processed with the standard pipeline and CALNICCR, one sees that the number of outliers is reduced. However, this is only half of the story; the uncertainty on the rate is an equally important ingredient in assessing the quality of the results. As discussed in § 3, the uncertainty necessarily increases for the pixels affected by CRs. (This is one of the arguments for using the measured count-rate error information in all photometric procedures.) Therefore, it is instructive to examine the images after the sky-subtracted count rates are divided by their estimated uncertainties. As shown in Figures 10*c* and 10*d*, there is a clear improvement in the case of CALNICCR. The sky regions of the new image are very uniform, indicating that the pixels that look like outliers in the count-rate images have correctly estimated uncertainties and are therefore consistent with the sky level on that scale. (Recall that a histogram of such an uncertainty-normalized image was shown in Fig. 2.)

To quantify the effect of CALNICCR on point-source photometry, we also performed a photometric study with a point source embedded in a real image at random locations. The PSF was generated using the Tiny Tim simulation model (Krist & Hook 2004). After the source was added to the image, PSF photometry was performed at its location to measure the flux. The procedure was performed for the same image processed with both the standard NICMOS pipeline and CALNICCR, over a range of input fluxes (PSF amplitudes). We then counted the fraction of times that the output flux was different from the input flux by more that 3 times the calculated uncertainty. The results are shown in Figure 11.

Several features are clear in the figure. The fraction of the photometric outliers is substantially larger for low source count rate than for the higher rates. This is to be expected, as the photometric fit is just as likely to converge on a random deviant pixel as on the true point-source signal when their fluxes are comparable. The fraction of outliers is roughly a factor of 2 less for CALNICCR than for the standard NICMOS pipeline. Most of the difference is due to the improvement in the CR processing algorithm.

5. CONCLUSIONS

We have improved the NICMOS pipeline processing in three areas: (1) We made the count uncertainty estimates substantially closer to being correct. (2) We improved the CR detection and rejection procedure. (3) We have corrected for spillover in the pixels neighboring cosmic rays.[7]

The improvements are most relevant for analyses in which accurate, optimal, and unbiased uncertainties are important, and for observations of faint objects, where subtle effects from CRs are important. For such cases, our new pipeline improves the photometric weight by ~30% in comparison with the standard NICMOS pipeline.

The relevance of our improvements for future space-based infrared instruments, such as those for the *James Webb Space Telescope* (*JWST*) or the Joint Dark Energy Mission (JDEM), depends on the amount of the readout noise the infrared arrays possess. Larger noise calls for more consideration to be given to the pipeline processing, and for more readouts during an exposure. Fortunately, modern NIR arrays possess substantially lower readout noise than those of NICMOS. Better CR handling will be important for the photometry of faint sources for *JWST* and JDEM, as the CR pollution rate will be worse than that experienced by the *HST*.

We are grateful to Eddie Bergeron, Howard Bushouse, Chris Bebek, Al Schultz, and Ralph Bohlin for discussions regarding the NICMOS features, performance, and calibration. We thank Tony Spadafora for feedback regarding the manuscript. We thank the anonymous referee for help in improving the clarity of the paper.

[7] The new code implementing these improvements, CALNICCR, is available at http://www-supernova.lbl.gov/~fadeyev/calniccr.tar.gz.

Partial support for this work was provided by NASA through grants from the Space Telescope Science Institute (STScI), associated with program numbers GO-8088 and GO-9075. STScI is operated by the Association of Universities for Research in Astronomy, Inc., under NASA contract NAS 5-26555. This work was also supported in part by the Director, Office of Science, Office of High Energy and Nuclear Physics, of the US Department of Energy, under Contract No. DE-AC03-76SF000098.

APPENDIX A

LINEAR FIT FORMULAE FOR UNCORRELATED DATA

Equations (A1)–(A4) are the linear fit formulae for uncorrelated data. The dependence of signal (photon counts) y_i on the readout time x_i is fit to the linear dependence y_i, and the count rate b is derived:

$$b = \frac{1}{\mathrm{Det}} (SS_{xy} - S_x S_y), \tag{A1}$$

$$\sigma(b) = \frac{1}{\sqrt{\mathrm{Det}}}, \tag{A2}$$

$$\mathrm{Det} = SS_{xx} - S_x^2, \tag{A3}$$

$$S = \sum_{i=1}^{n} \frac{1}{\sigma_i^2}, \quad S_x = \sum_{i=1}^{n} \frac{x_i}{\sigma_i^2}, \quad S_{xx} = \sum_{i=1}^{n} \frac{x_i^2}{\sigma_i^2},$$
$$S_y = \sum_{i=1}^{n} \frac{y_i}{\sigma_i^2}, \quad S_{xy} = \sum_{i=1}^{n} \frac{x_i y_i}{\sigma_i^2}. \tag{A4}$$

APPENDIX B

COUNT-RATE ERROR FOR THE CASE OF INTER-READOUT CORRELATIONS

Equations (B1)–(B5) present the count-rate estimate accounting for the inter-readout correlations:

$$\sigma(b) = \frac{1}{\Delta} \sqrt{\sigma(P)^2 + \sigma(G)^2}, \tag{B1}$$

$$\Delta = S_{xx} - S_x^2/S, \tag{B2}$$

$$\sigma(P)^2 = \sum_{k=2}^{n} S_k^2 \left(\frac{S_x}{S} - \frac{S_{xk}}{S_k}\right)^2 \frac{\delta y_k}{\mathrm{gain}}, \tag{B3}$$

$$\sigma(G)^2 = R^2 \sum_{k=1}^{n} \frac{1}{\sigma_k^4} \left(\frac{S_x}{S} - x_k\right)^2, \tag{B4}$$

$$S_k = \sum_{i=1}^{k-1} \frac{1}{\sigma_i^2}, \quad S_{xk} = \sum_{i=k-1}^{n} \frac{x}{\sigma_i^2}. \tag{B5}$$

Here the $\sigma(P)^2$ term comes from the Poisson part of the readout values, and $\sigma(G)^2$ is due to the Gaussian readout noise.

APPENDIX C

COUNT-RATE ERROR FOR PIXELS AFFECTED BY COSMIC RAYS

Here we fit both the readout sequences before and after a CR jump to linear functions with the same slope: $y_1 = a_1 + b \times \mathrm{time}$; $y_2 = a_2 + b \times \mathrm{time}$.

For the case of a single CR jump, we can define the joint χ^2 as follows:

$$\chi^2 = \sum_{i=1}^{k} \frac{[y_i - (a_1 + bx_i)]^2}{\sigma_i^2} + \sum_{i=k+1}^{n} \frac{[y_i - (a_2 + bx_i)]^2}{\sigma_i^2}. \tag{C1}$$

To minimize χ^2, we take partial derivatives with respect to a_1, a_2, and b, and equate them to zero:

$$\frac{\partial \chi^2}{\partial a_1} = \sum_{i=1}^{k} \frac{y_i - (a_1 + bx_i)}{\sigma_i^2} = 0, \tag{C2}$$

$$\frac{\partial \chi^2}{\partial a_2} = \sum_{i=k+1}^{n} \frac{y_i - (a_2 + bx_i)}{\sigma_i^2} = 0, \tag{C3}$$

$$\frac{\partial \chi^2}{\partial b} = \sum_{i=1}^{k} \frac{x_i[y_i - (a_1 + bx_i)]}{\sigma_i^2} + \sum_{i=k+1}^{n} \frac{x_i[y_i - (a_2 + bx_i)]}{\sigma_i^2} = 0. \quad \text{(C4)}$$

This is a system of linear equations with respect to a_1, a_2, and b. We introduce a superscript to the quantities S, S_x, S_{xx}, S_y, and S_{xy} defined in equation (A4) to differentiate sums over different parts of the readout sequence and rewrite the equations as follows:

$$a_1 S^1 + bS_x^1 = S_y^1,$$
$$a_2 S^2 + bS_x^2 = S_y^2,$$
$$a_1 S_x^1 + a_2 S_x^2 + b(S_{xx}^1 + S_{xx}^2) = S_{xy}^1 + S_{xy}^2. \quad \text{(C5)}$$

In the case of N CR jumps, the readout sequence will have $N + 1$ partitioned segments, the χ^2 will have $N + 1$ terms, and there will be $N + 2$ linear equations to solve for a_i and b. Nonetheless, the equations are simple enough to be solved manually. We derive the following expressions for b and a_i in the general case:

$$b = \frac{1}{\Delta} \sum_i (S^i S_{xy}^i - S_x^i S_y^i), \quad \text{(C6)}$$

$$\Delta = \sum_i [S_{xx}^i - (S_x^i)^2/S^i], \quad \text{(C7)}$$

$$a_i = (S_y^i - bS_x^i)/S^i. \quad \text{(C8)}$$

For the case of a single segment (no CR jump), equations (C6)–(C7) are reduced to (A1)–(A4).

For $\sigma(b)$ we derive an expression similar to equation (B1):

$$\sigma(b) = \frac{1}{\Delta} \sqrt{\textstyle\sum_i [\sigma(P)_i^2 + \sigma(G)_i^2]}, \quad \text{(C9)}$$

$$\sigma(P)_i^2 = \sum_{k=2}^{n_i} (S_k^i)^2 \left(\frac{S_x^i}{S^i} - \frac{S_{xk}^i}{S_k^i}\right)^2 \frac{\delta y_k}{\text{gain}}, \quad \text{(C10)}$$

$$\sigma(G)_i^2 = R^2 \sum_{k=1}^{n_i} \frac{1}{\sigma_k^4} \left(\frac{S_x^i}{S^i} - x_k\right)^2. \quad \text{(C11)}$$

REFERENCES

Bohlin, R., Lindler, D., & Riess, A. 2005, Grism Sensitivities and Apparent Non-Linearity (NICMOS ISR 2005-002) (Baltimore: STScI)

Bohlin, R., Riess, A., & de Jong, R. S. 2006, NICMOS Count Rate Dependent Non-Linearity in G096 and G141 (NICMOS ISR 2006-002) (Baltimore: STScI)

Bushouse, H. 1997, The STScI NICMOS Pipeline: CALNICA (NICMOS ISR 1997-028) (Baltimore: STScI)

Calzetti, D. 1997, Cosmic Rays on NICMOS: Results from On-Orbit Data (NICMOS ISR 1997-022) (Baltimore: STScI)

de Jong, R. S. 2006, Correcting the NICMOS Count-Rate Dependent Non-Linearity (NICMOS ISR 2006-003) (Baltimore: STScI)

de Jong, R. S., Bergeron, L. E., Riess, A., & Bohlin, R. 2006, NICMOS Count-Rate Dependent Non-Linearity Tests Using Flatfield Lamps (NICMOS ISR 2006-001) (Baltimore: STScI)

Figer, D. F., Rauscher, B. J., Regan, M. W., Morse, E., Balleza, J., Bergeron, L., & Stockman, H. S. 2004, Proc. SPIE, 5167, 270

Fixsen, D. J., Offenberg, J. D., Hanisch, R. J., Mather, J. C., Nieto-Santisteban, M. A., Sengupta, R., & Stockman, H. S. 2000, PASP, 112, 1350

Garnett, J. D., & Forrest, W. J. 1993, Proc. SPIE, 1946, 395

Garnett, J. D., et al. 2004, Proc. SPIE, 5499, 35

Gordon, K. D., et al. 2005, PASP, 117, 503

Hesselroth, T., Ha, E. C., Pesenson, M., Kelly, D. M., Rivlis, G., & Engelbracht, C. W. 2000, Proc. SPIE, 4131, 26

Heyer, I., & Biretta, J. A. 2005, WFPC2 Instrument Handbook, Version 9.1 (Baltimore: STScI)

Hodapp, K.-W., Rayner, J., & Irwin, E. 1992, PASP, 104, 441

Hodapp, K.-W., et al. 1996, NewA, 1, 177

Krist, J., & Hook, R. 2004, The Tiny Tim User's Guide, Version 6.3 (Baltimore: STScI)

Mobasher, B., & Riess., A. 2005, A Test of Possible NICMOS Non-Linearity (NICMOS ISR 2005-003) (Baltimore: STScI)

Mobasher, B., & Roye, E. 2004, NICMOS Data Handbook, Version 6.0 (Baltimore: STScI)

Offenberg, J. D., et al. 2001, PASP, 113, 240

Schultz, A., et al. 2005, NICMOS Instrument Handbook, Version 8.0 (Baltimore: STScI)

Skinner, C. J., et al. 1998, Proc. SPIE, 3354, 2

Sparks, W. B. 1998, Statistics of Accumulating Signal (NICMOS ISR 98-008) (Baltimore: STScI)

Thompson, R. I., Rieke, M. J., Kormos, K. A., & Mentzell, J. E. 1995, Proc. SPIE, 2475, 367

Thompson, R. I., Rieke, M., Schneider, G., Hines, D. C., & Corbin, M. R. 1998, ApJ, 492, L95

Williams, R. E., et al. 2000, AJ, 120, 2735